Polytype selection in the antisolvent-free crystallization of formamidinium lead iodide using alkylammonium chlorides

Journal:	*Journal of Materials Chemistry A*
Manuscript ID	TA-ART-01-2025-000577.R1
Article Type:	Paper
Date Submitted by the Author:	29-Apr-2025
Complete List of Authors:	Marchezi, Paulo; University of California San Diego, Aiiso Yufeng Li Family Department of Chemical and Nano Engineering Palmer, Jack; University of California San Diego, Materials Science and Engineering Program Hossain, Maimur; University of California San Diego, Aiiso Yufeng Li Family Department of Chemical and Nano Engineering Kodalle, Tim; Lawrence Berkeley National Laboratory, Molecular Foundry Division; Lawrence Berkeley National Laboratory, Advanced Light Source Moral, Raphael; Lawrence Berkeley National Laboratory, Molecular Foundry Division; University of Nevada Las Vegas, Nevada Extreme Conditions Laboratory Sutter-Fella, Carolin; Lawrence Berkeley National Laboratory, Molecular Foundry Division Fenning, David; University of California San Diego, Aiiso Yufeng Li Family Department of Chemical and Nano Engineering; University of California San Diego, Materials Science and Engineering Program

Polytype selection in the antisolvent-free crystallization of formamidinium lead iodide using alkylammonium chlorides

Paulo E. Marchezi[1‡], Jack R. Palmer[2‡], Maimur Hossain[1], Tim Kodalle[3,4], Raphael F. Moral[3,5],
Carolin M. Sutter-Fella[3], David P. Fenning[1,2]

[1]Aiiso Yufeng Li Family Department of Chemical and Nano Engineering, University of California San Diego, 9500 Gilman Drive, La Jolla, California 92093, United States.

[2]Materials Science & Engineering Program, University of California San Diego, 9500 Gilman Drive, La Jolla, California 92093, United States

[3]Molecular Foundry Division, Lawrence Berkeley National Laboratory, 1 Cyclotron Road, Berkeley, California 94710, United States.

[4]Advanced Light Source, Lawrence Berkeley National Laboratory, 1 Cyclotron Road, Berkeley, California 94710, United States.

[5]Nevada Extreme Conditions Laboratory, University of Nevada, Las Vegas, Las Vegas, Nevada 89154, United States

ABSTRACT

Understanding the nucleation, crystallization, and phase transition mechanisms in perovskite thin films produced without antisolvent quenching is crucial for improving phase stability and optoelectronic performance at scale. By means of *in situ* grazing incidence wide-angle X-ray scattering experiments, we show that the nature of alkylammonium chloride (RACl) additives significantly influences the crystallization dynamics and temperature-dependent stability of formamidinium lead iodide ($FAPbI_3$) perovskite films formed using antisolvent-free processes. The *in situ* experiments reveal that the effective radius of the RA^+ cation and the vapor pressure of the RA^0 conjugate base are critical factors affecting the crystallization pathway and film morphology. C_2-C_3 additives with moderate chain lengths may strike a balance between promoting the early crystallization of the cubic 3C phase while suppressing unwanted phases. This balance promotes the formation of highly crystalline cubic perovskite phase with well-oriented structure and better optoelectronic properties. These findings provide guidance regarding the design of additives to crystallize more stable and efficient perovskite films for optoelectronic applications.

KEYWORDS: perovskite, in situ GIWAXS, crystallization, intermediate, additive

INTRODUCTION

The high power conversion efficiency (PCE) of halide perovskite solar cells (PSCs) relative to thermodynamic limits[1] and their potential for low-cost and large-scale manufacturing through solution deposition techniques have attracted substantial interest across both academic and industrial spheres. Most of the highest-performing PSCs have a composition based predominantly on formamidinium lead iodide ($FAPbI_3$), culminating in a certified PCE of 26.1%.[2] However, $FAPbI_3$ absorbers exhibit phase instability. The photoactive α-$FAPbI_3$ phase is thermodynamically stable at temperatures above 390 K. Below this temperature, a non-photoactive phase, δ-$FAPbI_3$, is favored thermodynamically.[3,4] Thus, either the energy landscape must be altered via compositional, strain or additive engineering[4,5] or the black phase must be kinetically trapped.[4,6,7] Extensive efforts to stabilize $FAPbI_3$ at room temperature have been reported by alloying it with small amounts of Cs^+, MA^+, Rb^+ cations or Br^-,Cl^-, or $HCOO^-$ anions to form α-$FAPbI_3$-rich perovskites.[8] However, A- or X-site alloying alters the bandgap and cause local phase segregation, where nanoscopic phase segregation negatively affects stability.[9]

Alternatively, to maintain a nearly pure α-$FAPbI_3$ perovskite film while facilitating crystallization and stabilization into the α-phase, volatile additives can be added to the precursor, especially small alkylammonium chloride (RACl) salts.[10,11] Methylammonium chloride (MACl), in particular, has been widely demonstrated to improve nucleation and growth processes, thereby enhancing the crystalline quality of resultant perovskite films, while also increasing crystallographic texture and film uniformity.[10,12–16] On the other hand, MACl has critical downsides when used in perovskite solar cells, particularly in the presence of formamidinium (FA). The reaction between MA and FA in the precursor solution, or during annealing and over time in the solid state, can lead to the formation of N-methylformamidinium (nMFA), which affects the phase purity and crystallinity of the resulting perovskite films.[17,18] Moreover, because of the reactivity of perovskite precursor solutions containing MACl, they need to be used as soon as possible after preparation, as prolonged aging leads to significant performance drops, making the manufacturing process more challenging and less reproducible.

Using larger alkylammonium cations, such as ethylammonium chloride (EACl) or butylammonium chloride (BACl), can effectively reduce the aging of perovskite solutions by reducing the formation of degradation products. Although they have a pKa similar to methylammonium, the larger alkylammonium cations present greater steric hindrance and higher boiling point of their corresponding amines. These properties reduce the rate of nucleophilic attack on FA cations and volatilization of neutral amines, respectively.[19] This results in a more stable precursor solution and maintains the stoichiometric balance, which can enhance the quality of the perovskite films produced.[18] When using antisolvents to drive crystallization, it has been shown that the particular RA group can influence crystal growth, orientation, crystallinity, grain sizes, and uniformity.[20] For example, using a DMSO:DMF ink in an antisolvent process, Seok et al. found that adding isopropylammonium chloride (iPACl) in addition to MACl helps stabilize the α-phase, resulting in highly efficient and stable PSCs.[10] *In situ* photoluminescence studies of anti-solvent driven crystallization also showed that FACl and NH_4Cl reduce the formation temperature of α-$FAPbI_3$ relative to additive-free crystallization, but do not lower it as much as MACl does.[15]

In parallel, researchers have increasingly explored means to avoid anti-solvent driven crystallization of perovskite $FAPbI_3$, aiming to enable large-area processing and high-volume manufacturing. Researchers have demonstrated that by adjusting the ratio of a volatile, non-coordinating solvent to a Pb-coordinating, non-volatile solvent, compact perovskite thin films can be formed. Through controlled solvent evaporation, these films achieve optoelectronic and crystalline quality comparable to those produced via traditional antisolvent processing.[21,22] Without an antisolvent driving crystallization, the precise crystallization pathway and film-level property effects of alkylammonium cations can be expected to be distinct, as the amines strongly interact with the perovskite constituents and the RACl cations may be included in the final film to varying extent.[10,16,23]

To investigate how alkylammonium chloride (RACl) additives alter antisolvent-free crystallization dynamics and the phase stability of lead-halide perovskite films, we examine here a systematic series of RACl additives from NH_4Cl to BACl (C_0-C_4). The application of *in situ* characterizations has been proven essential in comprehending the crystallization processes of complex materials,[24,25] including halide perovskites. Specifically, *in situ* grazing incidence wide angle X-ray scattering (GIWAXS) has been valuable to reveal the transient crystalline phases present during film fabrication.[26,27] Here we apply *in situ* GIWAXS measurements to reveal how the alkylammonium chloride additives determine the dynamics of crystallization in the anti-solvent free deposition of $FAPbI_3$. We find that the ionic radius of the RACl governs the sequential evolution of polymorphs to yield α-$FAPbI_3$, while the chain length determines the residual RA present in the final film and its propensity to form 2D phases. Finally, we discuss the design of perovskite crystallization for scalability, focused on tailoring the polymorph transitions in the crystallization mechanism and then optimizing processing conditions to maximize the benefits in practical applications.

METHODS

Materials

Isopropanol (HPLC grade), acetone (HPLC grade), Hellmanex III, 2-methoxyethanol (99.8%, anhydrous), 1-methyl-2-pyrrolidone (99.5%, anhydrous), ammonium chloride (99.998% trace metals basis), (3-aminopropyl)triethoxysilane (99%), and ethanol (200 proof, anhydrous) were purchased from Sigma Aldrich. PbI_2 (99.99% trace metals basis), isopropylammonium chloride (98.0+%), n-propylammonium chloride (98+%), n-butylammonium chloride (98+%), and MeO-2PACz (98+%) were purchased from TCI America. Formamidinium iodide, ethylammonium chloride, and methylammonium chloride were purchased from Greatcell. The above chemicals were used as received without further modification. All substrates were treated with the following procedure before deposition: 15-minute sonication in DI H_2O, acetone, and IPA followed by a 20-minute UV-Ozone treatment. After cleaning, we spun coat on top of all 10x10mm ITO substrates (Biotain Crystal Co., Limited), a 0.6 mg mL^{-1} solution of MeO-2PACz in ethanol at 3000 rpm, 500 rpm/sec for 30 sec, with subsequent annealing at 100 ˚C for 10 min.

Precursor solution preparation

To prepare the perovskite precursor solution, the respective amounts of PbI_2 and FAI were weighed to prepare a 1.33M $FAPbI_3$ perovskite solution and dissolved in 2-ME by vortexing in a 4 mL vial. In a second vial, the desired amount of the RACl salt is weighed (7.5, 15.0, and 22.5

mol %). Then the perovskite solution was added to the vial containing the RACl and allowed to dissolve. After dissolving, 7.5% v/v of NMP is added to the solution.

Film preparation

The perovskite films were deposited by spin coating at 5000 rpm for 30 s under nitrogen. The custom spin coater is attached to the end station of beamline 12.3.2 at the Advanced Light Source (ALS), Lawrence Berkeley National Laboratory. The spin coater setup is designed such that the experiment can be performed remotely, avoiding any transfer delays between film deposition and annealing. After spin coating, samples were heated using a temperature ramp of about 4.5 °C s^{-1} to 150 °C. The annealing temperature was held for 10 min and then the sample was left to cool down to ambient temperature.

Characterization

GIWAXS data was collected during spin coating of thin films and thermal annealing to follow the crystallization process. The incident X-ray beam was held at a shallow angle of 1° with a beam energy of 10 keV. A DECTRIS Pilatus 1M X-ray detector was placed at an angle of 35° to the sample plane and a sample-to-detector distance of ~189 mm was used. The beam projection was on an area of 575 μm^2 (115 μm × 5 μm) with an approximate flux of $\sim 10^9$ photons s^{-1}. The scattering detector distance (SDD) was calibrated using an Al_2O_3 powder standard prior to the experiment, and the detector position remained fixed throughout. Additionally, before the *in situ* fabrication of each sample, diffraction from the bare ITO substrate was collected. This ITO diffraction data was also used for SDD calibration for each sample. The diffraction data was collected with a frame rate of 0.56 s^{-1}. The 2D diffraction images were initially analyzed using custom-made software and then further analyzed by using pyFAI and pygix python packages.[28]

Ex-situ X-ray diffraction measurements were carried out using an Anton Paar XRDynamic 500 in Bragg-Brentano beam geometry, and coupled scans were taken from 3°-45° 2θ. Photoluminescence (PL) spectra was taken using a 0.9 mW 635 nm laser (Thorlabs) as an excitation source. Spectra were collected through a 200 μm slit grating thermoelectric-cooled spectrometer (StellarNet SILVER-Nova). Scanning electron micrographs were collected in secondary electron imaging mode using in-lens detection on an FEI Apreo SEM, with beam energy and current fixed at 2kV and 50pA respectively.

RESULTS AND DISCUSSION

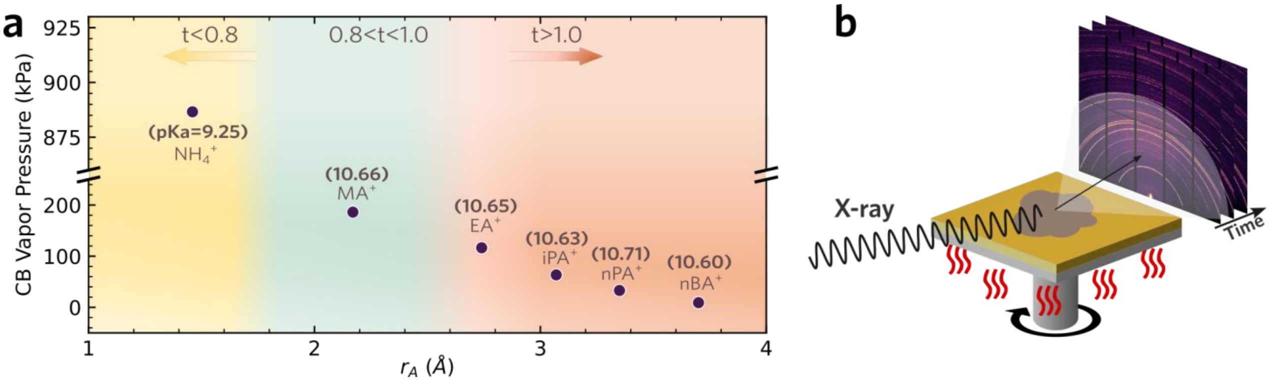

Figure 1: (a) NH$_4^+$, MA$^+$, EA$^+$, iPA$^+$, nPA$^+$, and BA$^+$ cations (RA) used in this work, classified by their cationic radius and corresponding vapor pressure of the conjugate base (CB). (b) Schematic illustration of the *in situ* characterization setup used during FAPbI$_3$ thin film deposition.

In situ GIWAXS was used to monitor the crystallization process during the spin coat deposition of 2-ME/NMP based FAPbI$_3$ inks. These inks allow for the crystallization of cubic perovskite films without the use of an anti-solvent or air knife. Such films can achieve >10% PLQY.[19] A series of additions of NH$_4^+$, MA$^+$, EA$^+$, iPA$^+$, nPA$^+$, and nBA$^+$ chloride salts of 7.5, 15, and 22.5 mol% relative to FAPbI$_3$ were investigated to study how the characteristics of the alkylammonium chloride additive affect the crystallization. For comparison, films with no RACl additives were also included (labeled control), as were inks without any of the coordinating NMP solvent.

In Figure 1a, we organize the additives according to their effective ionic radius (r_A)[29–31] and corresponding vapor pressure of the conjugate base (CB); two related parameters expected to play a key role in determining the effect on the crystallization process by indicating the rate at which the additive leaves the film and where it will crystallize if it remains. In Figure 1a, the RACls are separated into three distinct regions according to their approximate Goldschmidt tolerance factor (t) in the perovskite phase. MA^+ exists in the central green region where $0.8<t<1.0$ and cations can fit in the A-site of the cubic perovskite lattice without significant distortion. The yellow (left, $t<0.8$) and the orange (right, $t>1.0$) regions represent cations with smaller and larger r_A than the ideal size for a cubic perovskite lattice, respectively. NH_4^+ is too small, EA^+ is right on the edge of too big, and longer chained alkylammonium cations iPA^+, nPA^+, and nBA^+ cations are too big to fit in the A-site of a cubic perovskite lattice.

The crystallization dynamics of each additive in the anti-solvent free deposition of perovskite films were characterized by *in situ* GIWAXS during spin coating and annealing, using the experimental setup developed at the Beamline 12.3.2, at the Advanced Light Source synchrotron. The experimental design and setup are shown schematically in Figure 1b.

Figure 2 presents the *in situ* GIWAXS during the initial 200 seconds of the film deposition process for films with 15 mol% MACl, EACl, iPACl, and nPACl. To facilitate readability, NH_4Cl and BACl are included for reference in the SI. The top row in each subpanel in Figure 2 shows the spin coater speed vs. time. The middle presents scattering intensity heat maps showing the evolution of diffraction intensity (on a logarithmic scale) as a function of time and scattering vector, q (Å^{-1}). The bottom row provides the time evolution of selected diffraction peaks, highlighting the dynamics of the crystalline phases during spinning and the temperature rise to the annealing temperature. Full scattering data are provided for the 7.5, 15, and 22.5 mol% films in Figures S1-S7. We divide the results and discussion below into stages: (1) following the progression from sol and intermediates at the earliest times, (2) the evolution to the 3C perovskite phase, and finally (3) the crystal evolution during the completion of a standard annealing step.

Intermediate Formation upon Deposition

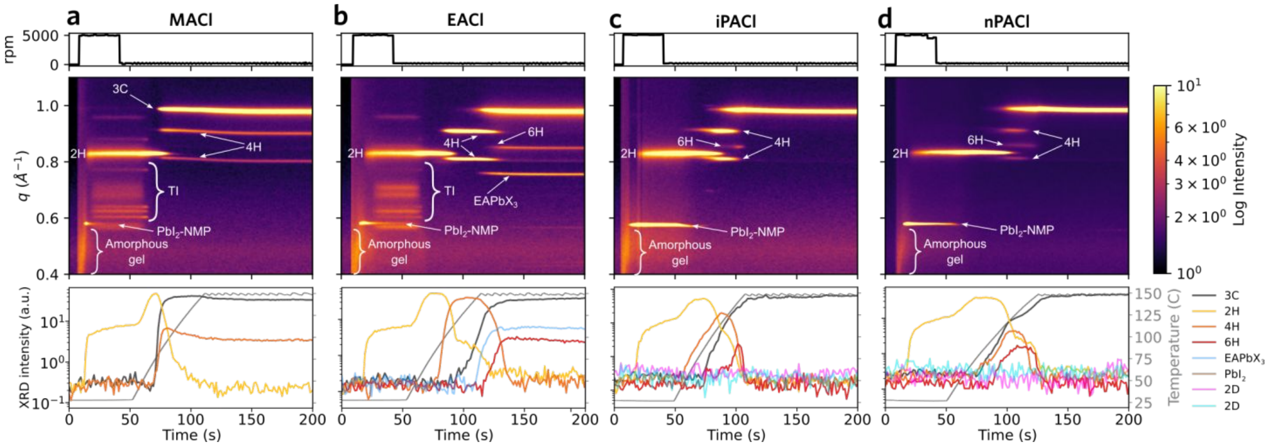

Figure 2: (Top) Heat map of azimuthally integrated *in situ* GIWAXS over the first 200s of the film deposition process for films containing 15.0 mol% of (a) MACl, (b) EACl, (c) iPACl and (d) nPACl. (Bottom) The time evolution of selected diffraction peaks, extracted from the corresponding GIWAXS results.

For the first 5 s after the start of the spinning process for all inks, the scattering data indicate a lack of crystalline phases (Figure 2). Instead, only scattering from a colloidal sol-gel suspension lacking long-range order is detected. This suspension consists of dissolved precursors and solvents scattering around $q \approx$ (0.45-0.50) Å^{-1}.[32,33] The formation of this colloidal suspension (Amorphous gel) was observed regardless of the presence or absence of RACl (Figures S1-S8).

The formation of crystalline phases was observed around 6 s after the spin coating process began. As seen in Figure 2, a crystalline peak appears at 0.58 Å^{-1}, early in the spin-coating process, from the PbI_2(NMP) intermediate. Composed of PbI_2 bi-lamellae spaced by NMP solvent molecules, the intermediate has large interplanar spacings and therefore low q.[34–36]

In the films with MACl, or with EACl, a complex set of diffraction peaks between 0.6 and 0.7 Å^{-1} emerge at ~19 seconds into the process that we term "transitional intermediates" (denoted 'TI' in Figure 2a), which is also present in samples with no additive (Figure S1c). We note that without NMP, the PbI_2(NMP) peak and the transitional intermediates between 0.6 and 0.7 Å^{-1} did not form, regardless of the presence of RACl (Figure S1a, b). Thus, the scattering phases of the transitional intermediates are likely composed of mixed cations and anions with solvent or additive molecules (solvent complex).[35,37,38] It is likely that the TIs are composed mainly of an FAI-PbI_2-NMP complex[39], with some variation in the exact scattering peaks depending on interactions with the specific additive in that sample. For MACl and EACl, we observe transition intermediates with a range of q values extending slightly larger than without the additive (0.5-0.7 Å^{-1}). EACl has only a slightly larger r_A than MACl (Figure 1a).

The concentration of the RACl influences the appearance of the transitional intermediates between 0.6 and 0.7 Å^{-1} (Figures S2-S8). At 7.5 mol%, all RACls present the intermediates at 0.6 and 0.7 Å^{-1} during the spin coating step (Figures S2a-S8a). At 15.0 mol%, it is only present in the films with smaller cations, MA^+ (Figure S3b) and EA^+ (Figure S4b). With the larger iPA^+, nPA^+

and nBA^+, we did not observe the transitional intermediates in samples with 15 mol% additive (Figure 2c, d and Figure S7b). For these cations, the amorphous gel is converted to the 2H and PbI_2-NMP intermediate phases. Without NMP or RACl (Figure S1a) the 2H $FAPbI_3$ phase forms immediately upon initiation of spin coating, indicating a rapid crystallization process.

In this phase of the film formation, the interaction of the ions and solvent molecules plays the most important role. NMP has a strong interaction with both FAI and PbI_2 to form the FAI−PbI_2−NMP structure in the perovskite precursor.[39] When we increase the size or concentration of the RA additives, we disrupt this interaction as we do not see the appearance of the transitional phase for cations larger than EA^+ or higher concentrations (Figure 2 and S2-S7).

Conversion of Intermediates to 2H $FAPbI_3$

During the ramping of temperature at the onset of annealing, a sequence of phase changes occurs that fully converts the intermediate phases to crystalline 2H $FAPbI_3$. The PbI_2(NMP) peak at 0.58 $Å^{-1}$ disappears along with any intermediates between 0.6 and 0.7 $Å^{-1}$, if present (Figure S1-S7). Concomitantly, there is a brief increase in intensity of the 2H peak for all samples (Figures S2, bottom panels), suggesting that these intermediate phases are fully converted to the 2H phase at the beginning of the annealing process.

The temperature at which the complete transition to 2H occurs depends on the additive. For the sample without any additive, the transitional intermediates between 0.6 and 0.7 $Å^{-1}$ disappear at 63˚C, followed by the disappearance of PbI_2(NMP) around 112˚C. When these phases vanish, there is an increase in the intensity of the 2H hexagonal polytype. When MACl is added to the precursor solution, the PbI_2(NMP) and the transitional intermediates are converted to the 2H phase at around

60˚C. The intermediate phases totally convert to the 2H phase at 57˚C for EACl. For the longer RACls, which showed no transitional intermediates, the full conversion to the 2H occurs at higher temperatures: for nPACl full conversion to 2H happens at around 70˚C; for iPA and nBA it happens only above 90˚C. We speculate that this trend is caused by the steric bulk of larger additives preventing the full formation of the FAI-NMP-PbI_2 intermediate, leading to a longer-lived PbI_2-NMP intermediate. This trend could also possibly be due to the monotonic trend in additive vapor pressure with alkyl chain length: larger alkylammoniums stay in the film at higher temperatures, delaying the full conversion to 2H $FAPbI_3$. Further, the longer chain alkylammoniums appear to destabilize the 2H $FAPbI_3$, resulting in a phase transition to 4H and 6H polytypes. The larger cations may not fit well within the 2H lattice, causing the polytypes with larger cages to be favored.[40]

Phase Evolution to the 3C Phase

As the temperature continues to increase during annealing, the 3C phase becomes increasingly favored relative to the 2H phase, but the phase transition temperature and the emergence of other hexagonal polymorphs depends distinctly on the RACl additive. In the control sample with no additive (Figure S1c), the scattering heat map reveals distinct diffraction peaks corresponding to specific crystalline phases that form over time. It shows the development of 3C, 2H, and PbI_2 phases. This baseline data serves as a reference to understanding the impact of various additives on the crystallization process. We observe that without any RACl the 2H phase remains until the temperature rises to ~123˚C, when the 3C perovskite phase starts to be formed. The 2H phase is completely converted to the 3C phase at around 130˚C. However, right after the formation of the 3C phase, we see decomposition begin within seconds with the appearance of the PbI_2 at 145˚C.

The introduction of MACl leads to a decrease in the temperature where the 3C phase starts to appear, to around 75˚C (Figure 2a). This behavior aligns with previous reported results from studies of anti-solvent driven crystallization in the literature, where the addition of the MACl promotes the formation of 3C phase at lower temperatures.[10,14,15,37] This transformation from 2H to 3C occurs with the simultaneous appearance of the additional 4H hexagonal polytype (Figure 2a). The persistent presence of a minor fraction of 4H phase throughout the annealing process might be associated with the degradation of the MA-containing precursor solution, a phenomenon previously reported in the literature.[17,41] Notably, no PbI_2 is detected during the evolution to the 3C phase at short times during annealing with the MACl additive.

The EACl-assisted crystallization process exhibits distinctive behavior as the temperature rises during the annealing process, as seen in Figure 2b. There is a notable transition from 2H to 4H at 89˚C, and then to 3C, 6H, and $EAPbX_3$ phases above 130˚C. This distinct pathway is attributed to the differences in size and CB vapor pressure of EA^0. Additionally, EA^+ is larger than what would ideally fit within the cubic perovskite lattice. The intermediate size of EA^+ may lead to a competitive interaction among various hexagonal polytype intermediates, culminating in the formation of a mixture of 3C and hexagonal polytypes.

The trend toward a sequence of phase transitions through higher hexagonal polymorphs continues when employing the larger RACl additives, characterized by low vapor pressure and higher r_A. For the iPACl film of Figure 2c, the GIWAXS analysis reveals that the hexagonal 4H phase materializes initially at an onset temperature of 56˚C, preceding the formation of the cubic 3C phase. As the temperature rises to 75˚C, the 3C phase begins to emerge and steadily increases in intensity. As the temperature approaches 90˚C, the 4H phase is converted into both the 6H and 3C phases. At temperatures above 150˚C, the remaining 6H phase completely converts to the 3C phase.

The 3C phase formed in the iPACl film exhibits notable thermal stability throughout the annealing process, maintaining its structure without any detectable decomposition to PbI_2. This stability is crucial for the performance and longevity of perovskite-based devices. Moreover, in the specific case of iPACl as an additive, there is no evidence of two-dimensional (2D) perovskite phases at the beginning of the annealing process, suggesting a direct pathway to the 3C phase without intermediate 2D phase formation. This behavior contrasts with the nPACl and BACl additives that promote earlier formation of intermediate 2D phases discussed below, underscoring the unique influence of iPACl on the perovskite crystallization process.

nPACl and nBACl show a rather similar phase evolution to iPACl during heating from 2H to a mixture of phases. In the case of nPACl and nBACl, 4H, 3C and 6H phases emerge in rapid succession and coexist after reaching ~105˚C, until 3C becomes the sole phase at 150˚C. In contrast to iPACl, longer chain RACl additives nPACl and nBACl show a pronounced formation of 2D perovskite phases during annealing. This is evident from the diffraction peaks observed at 0.4 and 0.5 $Å^{-1}$ in Figure S6 and S7. For example, in the nBACl sample (Figure S7), the 2D phase starts to appear as the temperature reaches 150˚C. This early formation of 2D phases contrasts with the behavior of iPACl, which does not exhibit such phases initially. This can be rationalized by 1) the lower vapor pressure of long-chain alkylammoniums, slowing their release from the film during annealing and 2) the negative formation energy of 2D phases with longer-chain alkylammonium cations.[42] For additional comparison, the phase evolution of films with NH_4Cl as an additive is discussed in the Supplementary Note 1.

Impact of the Annealing Step

Having considered the phase evolution during the ramping to the annealing temperature, we now consider how the crystalline phases evolve during the full 10 min annealing and subsequent cooling. Figure 3 presents a comparison of the evolution of the azimuthally integrated GIWAXS patterns for MACl, EACl, iPACl, and nPACl additives through the annealing process.

A comparison between the no additive sample (Figure S1c) and the MACl additive sample (Figure 3a) reveals several notable distinctions. In the no additive sample, an increase in the PbI_2 peak is observed throughout the annealing process, indicating ongoing decomposition. Conversely, the addition of MACl delays the appearance of the PbI_2 peak, although there is still an increase in the presence of hexagonal polytypes, particularly the 4H phase (note that the 4H and PbI_2 diffractions are close together at ~0.91 and 0.89 $Å^{-1}$, respectively). This suggests that, while MACl favors the formation of 3C phase at lower temperatures, it also is similar in energy with hexagonal phases, which may contribute to the film's instability.

The addition of EACl (Figure 3b) results in significant changes in the dynamics of phase evolution during the annealing of $FAPbI_3$ films. Specifically, the 6H phase gradually decreases during annealing, while there is a slight increase in the intensity of the 3C phase peak, alongside a small increase in the 2H phase closer to the end of the process. Additionally, the peak associated with the $EAPbX_3$ perovskite, around 0.75 $Å^{-1}$, persists until the end of annealing. As the temperature begins to decrease, this peak splits into two distinct peaks, which are associated with high-n quasi-2D perovskite phases. This behavior underscores the complex phase interactions facilitated by EACl, where the balance between cubic and hexagonal phases is maintained throughout the annealing process.

For samples with iPACl (Figure 3c), an interesting phase evolution is observed during annealing. Two distinct peaks increase in intensity at low q-vector values, indicative of the formation of 2D perovskite phases. Notably, no PbI_2 peak emerges, and while trace amounts of hexagonal polytypes such as 6H, 4H, and 2H are present, their peak intensities only slightly increase, without any reduction in the 3C phase peak. This suggests that iPACl effectively stabilizes the 3C phase while also promoting the formation of minor 2D phases, contributing to the overall structural integrity of the film. We note that the small but abrupt change in q at around 700s is related to a contraction of the thermal paste used in the *in situ* setup hardware leading to a change in sample height and does not indicate a shift in lattice parameter.

The effect of nPACl during the annealing process (Figure 3d) differs notably from the other additives. There is no significant increase in the 2H, 4H, or 6H phases during annealing, although there is a clear increase in the 2D perovskite phase peak at 0.56 Å⁻¹. As the temperature decreases to around 125˚C, there is an abrupt increase in the peak at approximately 0.47 Å⁻¹, also associated with a 2D phase. At this stage, peaks corresponding to the 2H and 6H phases, around 0.80-0.85 Å⁻¹, also appear in trace quantity. This suggests that nPACl promotes the formation of 2D phases while largely suppressing the growth of hexagonal polytypes and PbI_2.

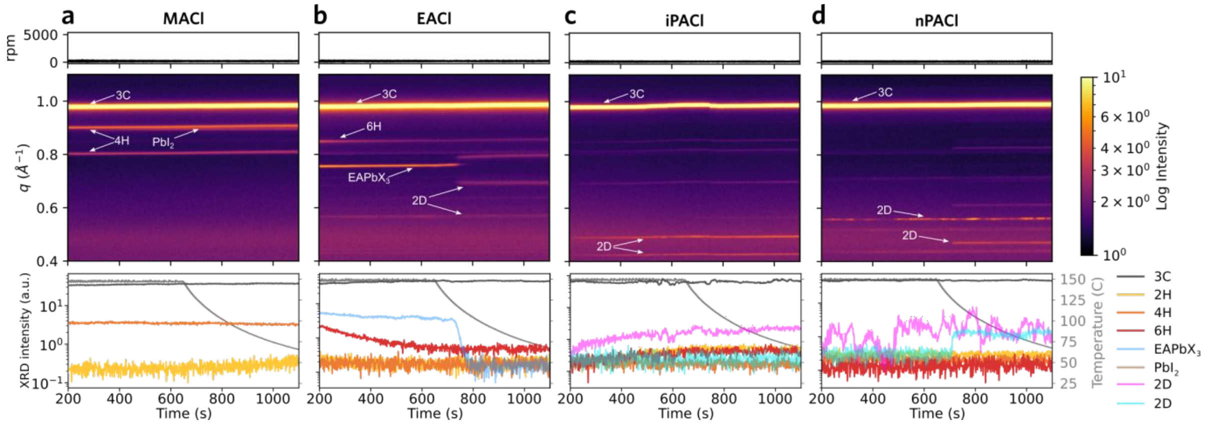

Figure 3: Heat map of azimuthally integrated *in situ* GIWAXS over the annealing step of the film deposition process for films containing 15.0 mol% of (a) MACl, (b) EACl, (c) iPACl, and (d) nPACl. (Bottom) The time evolution of selected diffraction peaks, extracted from the corresponding GIWAXS results.

The GIWAXS pattern evolution for the nBACl additive (Figure S7) is particularly notable for the pronounced increase in the signal around 0.55 Å⁻¹, associated with an nBA-based 2D perovskite phase. Given that the nBA^+ cation is widely used as a large A-site cation to form 2D perovskites, the formation of 2D phases during the process is anticipated. The increase in the peak related to the 2D phase occurs without a corresponding decrease in the 3C peak. Additionally, there is a small increase in the amount of the 2H phase toward the end of the film deposition process, suggesting minor degradation. The impact of the annealing step on the films modified with NH_4Cl is discussed in the Supplementary Note 1.

Summarizing Understanding of the Phase Evolution to form 3C Perovskite during Annealing

Figure 4a presents a summary of the temperatures at which the main crystalline phases emerge during the annealing of samples containing 15.0 mol% of various additives, as extracted from the GIWAXS results. This data offers valuable insights into the influence of additive size on the thermal evolution of perovskite phases. The data shows that, as we move from the control sample (without additive) to the sample modified with MACl, there is a noticeable decrease in the temperature at which the 2H phase disappears (top of the yellow bar). This trend is reversed with the introduction of larger cations, where the temperature required for the removal of the 2H phase begins to increase again. This behavior underscores the critical role of cation size in dictating the thermal stability of specific perovskite phases.

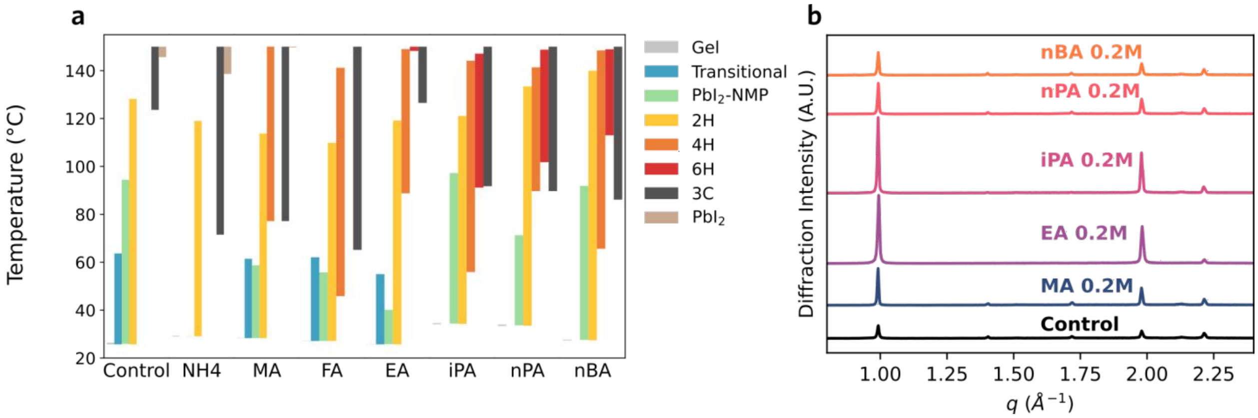

Figure 4: (a) Range of temperatures over which the phases are observed in the GIWAXS patterns. (b) Ex-situ diffraction patterns for $FAPbI_3$ films cast from inks without additive (Control) and 15.0 mol% RACl additives highlighting the large difference in diffraction intensity.

In addition to affecting the stability of the 2H phase, the size of the additive also influences the appearance of other hexagonal phases during annealing. As the size of the additive increases, we observe the emergence of new hexagonal polytypes. For instance, the 4H phase becomes apparent when MACl is used as an additive, while the 6H phase emerges with the introduction of EACl. With larger size of the additives, there is a temperature range during the annealing where all the hexagonal polytypes coexist, and this coexistence range shifts to higher temperatures for larger RACl additives. This observation highlights the complex interplay between additive size and phase evolution, where larger additives promote the formation of more complex hexagonal phases during the annealing process.

Another key finding from Figure 4a is the effect of additives on the temperature at which the 3C cubic phase appears. Across the board, the presence of an additive leads to a decrease in the temperature at which the 3C phase emerges, as compared to the control sample. However, the behavior of the sample containing EACl stands out. EACl's size appears to be at a critical ionic radius point where it can just stabilize the cubic phase (Figure 1). This is evident from the GIWAXS results, which shows that EACl stabilizes the 4H during annealing, thereby delaying the formation of the 3C phase and enabling competitive formation of the 6H phase. The presence of EA promotes the formation of an equilibrium between the 4H, 2H, and 3C phases at around 120˚C (Figure 2c). This is related to its intermediate ionic radius (Figure 1a). Then, it transforms to 3C and the 6H phase together with $EAPbX_3$ perovskite (Figure 2c).

The presence of yet larger additives facilitates the existence of the hexagonal polytypes for longer times and higher temperatures. As mentioned above, the presence of large alkyl chain cations hinders the formation of the FAI−PbI_2−NMP phase (Figure 2), but the residual RA can fit inside the oval-like A-site cages in the face-sharing hexagonal polytypes.[40] The size of the cation also influences the kind and intensity of the hexagonal phases formed when the sample is annealed. For larger cations (iPA^+, nPA^+, and nBA^+) the 4H phase appears at lower temperature, its intensity is gradually lower as we increasing the alkyl chain length (Figure 2c-d). Because of r_A size, these cations do not properly fit in the A site cage of the 4H polytype, and the phase progression follows from 4H to 6H and 3C phases with increasing temperature.

Additives with higher volatility, like iPACl, facilitate the formation of stable 3C phases without early formation of 2D phases, while those with lower volatility, like nPACl and nBACl, promote the formation of 2D phases early in the annealing process.[19] The r_A size influence is most dramatic for the nBA^+, where we observe the appearance of 2D perovskite phases shortly after the emergence of the 3D phase (Figure S7).

For comparison, Figure 4b shows the benchtop diffraction patterns for $FAPbI_3$ films cast from inks with 15 mol% and without additives, highlighting the large difference in diffraction intensity and as a function of additive. It is observed that EA^+ and iPA^+ yield films with higher 3C (100) peak intensity, when compared with films modified with the other additives (Figure 4b and Figure S8). This was further analyzed from the 2D diffraction patterns in Figure S8 and azimuthal intensity profiles in Figure S9. The films with EA^+ and iPA^+ cations present a higher out-of-plane diffraction intensity, which shows a preferential orientation of these perovskite films. The films formed with medium-sized RACl cations also present a slightly higher PL intensity (Figure S10), which suggests the formation of a perovskite film with less defects. For reference, the intensity and trends of the PL spectra shown in Figure S10 closely match our previously reported results for samples prepared under the same conditions reported here, where PLQY >10% under 1-sun injection was observed for the medium-sized RACl additives.[19] We see in Figure S11a-f that the morphology of the films containing 15 mol% additive present fewer pinholes than the films without additive (Figure S11g). MACl and EACl films have the least number of pinholes and largest apparent domain sizes among all. The *in situ* GIWAXS data indicates that the 3C phase forms in these films after an evolution through the higher hexagonal polytypes (4H and 6H). This early conversion from the 2H evolution to the 4H and 6H phases appear to promote a strong templating in the 3C phase when it forms. The favorable crystallographic templating between 6H and 3C polytypes has been highlighted recently.[43] However, as the alkyl chain length increases in nPA and nBA, the crystallinity of the films decreases, likely because the larger additive molecules partially disrupt the conversion to the 3C phase by strongly stabilizing the 6H and leading to the formation of lower-dimensional phases. The varied behaviors of these additives highlight the intricate influence of their conjugate base vapor pressure and ionic radii on the phase evolution and stability of the resulting perovskite films, underscoring the critical role of additive properties in determining the crystallization pathway and thermal stability. Notably, larger additives promote the sequential formation of more complex hexagonal phases during the annealing process, reflecting a complex interplay between additive size and phase evolution.

SUMMARY AND CONCLUSIONS

In this work, we investigated the role of C_0-C_4 alkylammonium chloride additives on the antisolvent-free crystallization of $FAPbI_3$ perovskite films using *in situ* GIWAXS. From ammonium to n-butylammonium chlorides, each additive distinctly influences the phase behavior, impacting both the temperature at which phase transformations occur and the stability of the resultant phases. The formation of crystalline intermediate solvent complexes, such as the PbI_2(NMP) and FAI-PbI_2-NMP phases, occurs in seconds during spin coating and only when the RACl cation is small (MA^+, EA^+) and in low concentration. As the temperature increases during annealing, these intermediate phases transform first into the 2H phase, and then, depending on the additive, through 4H and 6H polytopes and eventually into the 3C cubic phase.

EACl and iPACl show unique effects on the phase transition process and lead to highly crystalline films with strongly preferred (100) orientation. EACl promotes the formation of 4H hexagonal polytype at low temperatures, while iPACl leads to the early appearance of the 4H phase and the subsequent development of both 6H and 3C phases. In contrast, additives nPACl and nBACl proceed through a rapid transition with phase coexistence from 2H → 4H→ 6H → 3C but also show the formation of 2D perovskite phases quickly after the formation of 3C.

The study underlines how RACl additives can be selected based on their varying volatility and effective radii to direct the crystallization pathway of $FAPbI_3$ to avoid or pass through targeted intermediates and polytypes. The progression of crystallization through a 6H intermediate appears to correlate with the formation of highly crystalline, oriented 3C thin film and a suppression of hexagonal phases after annealing. Alkylammonium cation concentration and chain length further control the emergence of quasi-2D second phases. In this simple series of alkylammonium chlorides, rich phase behavior is observed in the progression of antisolvent-free crystallization that ultimately strongly determines the quality of the cubic perovskite and its phase stability, emphasizing the complex interplay between kinetic and thermodynamic factors in the crystallization process of these materials.

Importantly, we observed that the graded transition through hexagonal intermediates facilitated by cations larger than MA appears to enable a gradual evolution from fully face-sharing (2H) to increasingly corner-sharing polymorphs (4H, 6H), ultimately culminating in the fully corner-sharing 3C α-$FAPbI_3$ cubic phase. This progressive "easing" into corner-sharing connectivity is hypothesized to enhance crystal quality in the final film by reducing strain and promoting uniformity during the phase transformation process. The suppression of residual hexagonal phases and the preferred orientation of the cubic perovskite phase suggest that such a transition pathway may also play a critical role in improving phase stability observed in film-level degradation studies under 1-sun illumination and heating.[19] These observations underscore the value of exploring kinetic and thermodynamic pathways in the crystallization of perovskites and warrant further investigation into how these graded transitions can be leveraged to optimize both film quality and device performance.

Conflicts of Interest

There are no conflicts to declare.

Data Availability

Data is available upon reasonable request.

Author Contributions

‡These authors contributed equally to this work.

Acknowledgements

This work was supported by the U.S. Department of Energy, Office of Science, Office of Basic Energy Sciences under Award Number DE-SC0023484. T.K. acknowledges funding by the US Department of Energy (DOE), Office of Science, Office of Basic Energy Sciences, Materials Sciences and Engineering Division, under contract no. DE-AC02-05-CH11231 (D2S2 program KCD2S2). R.F.M. acknowledges the support of Chemical Sciences, Geosciences and Biosciences Division, Office of Basic Energy Sciences, Office of Science, U.S. Department of Energy under DOE Grant no. DE-SC-0023355. Part of the work was carried out as a user project at the Molecular Foundry, a user facility supported by the Office of Science, Office of Basic Energy Sciences, of the U.S. Department of Energy under Contract No. DE-AC02-05CH11231. Work at the Advanced Light Source (ALS) was done at beamline 12.3.2, where we gratefully acknowledge the support of Nobumichi Tamura. The ALS is a DOE Office of Science User Facility under contract no. DE-AC02-05CH11231.

REFERENCES

(1) Ehrler, B.; Alarcón-Lladó, E.; Tabernig, S. W.; Veeken, T.; Garnett, E. C.; Polman, A. Photovoltaics Reaching for the Shockley–Queisser Limit. *ACS Energy Lett.* **2020**, *5* (9), 3029–3033. https://doi.org/10.1021/acsenergylett.0c01790.

(2) *Best Research-Cell Efficiency Chart.* https://www.nrel.gov/pv/cell-efficiency.html (accessed 2024-01-15).

(3) Liu, X.; Luo, D.; Lu, Z.-H.; Yun, J. S.; Saliba, M.; Seok, S. I.; Zhang, W. Stabilization of Photoactive Phases for Perovskite Photovoltaics. *Nat. Rev. Chem.* **2023**, *7* (7), 462–479. https://doi.org/10.1038/s41570-023-00492-z.

(4) Chen, T.; Foley, B. J.; Park, C.; Brown, C. M.; Harriger, L. W.; Lee, J.; Ruff, J.; Yoon, M.; Choi, J. J.; Lee, S.-H. Entropy-Driven Structural Transition and Kinetic Trapping in Formamidinium Lead Iodide Perovskite. *Sci. Adv.* **2016**, *2* (10), e1601650. https://doi.org/10.1126/sciadv.1601650.

(5) Yu, H.; Sun, Q.; Zhang, T.; Zhang, X.; Shen, Y.; Wang, M. Is the Strain Responsible to Instability of Inorganic Perovskites and Their Photovoltaic Devices? *Mater. Today Energy* **2021**, *19*, 100601. https://doi.org/10.1016/j.mtener.2020.100601.

(6) Zhao, Y.; Zhao, K.; Wan, L.; Tan, Y.; Wang, Z.-S. Black Phase of Inorganic Perovskite Stabilized with Carboxyimidazolium Iodide for Stable and Efficient Inverted Perovskite Solar Cells. *ACS Appl. Mater. Interfaces* **2022**, *14* (5), 6906–6915. https://doi.org/10.1021/acsami.1c23637.

(7) Jin, H.; Zeng, Y.-J.; Steele, J. A.; Roeffaers, M. B. J.; Hofkens, J.; Debroye, E. Phase Stabilization of Cesium Lead Iodide Perovskites for Use in Efficient Optoelectronic Devices. *NPG Asia Mater.* **2024**, *16* (1), 1–18. https://doi.org/10.1038/s41427-024-00540-0.

(8) Saliba, M.; Matsui, T.; Seo, J.-Y.; Domanski, K.; Correa-Baena, J.-P.; Nazeeruddin, M. K.; Zakeeruddin, S. M.; Tress, W.; Abate, A.; Hagfeldt, A.; Grätzel, M. Cesium-Containing Triple Cation Perovskite Solar Cells: Improved Stability, Reproducibility and High Efficiency. *Energy Environ. Sci.* **2016**, *9* (6), 1989–1997. https://doi.org/10.1039/C5EE03874J.

(9) Brennan, M. C.; Draguta, S.; Kamat, P. V.; Kuno, M. Light-Induced Anion Phase Segregation in Mixed Halide Perovskites. *ACS Energy Lett.* **2018**, *3* (1), 204–213. https://doi.org/10.1021/acsenergylett.7b01151.

(10) Park, J.; Kim, J.; Yun, H.-S.; Paik, M. J.; Noh, E.; Mun, H. J.; Kim, M. G.; Shin, T. J.; Seok, S. I. Controlled Growth of Perovskite Layers with Volatile Alkylammonium Chlorides. *Nature* **2023**, *616* (7958), 724–730. https://doi.org/10.1038/s41586-023-05825-y.

(11) Feng, W.; Tan, Y.; Yang, M.; Jiang, Y.; Lei, B.-X.; Wang, L.; Wu, W.-Q. Small Amines Bring Big Benefits to Perovskite-Based Solar Cells and Light-Emitting Diodes. *Chem* **2022**, *8* (2), 351–383. https://doi.org/10.1016/j.chempr.2021.11.010.

(12) Jiang, Q.; Chu, Z.; Wang, P.; Yang, X.; Liu, H.; Wang, Y.; Yin, Z.; Wu, J.; Zhang, X.; You, J. Planar-Structure Perovskite Solar Cells with Efficiency beyond 21%. *Adv. Mater.* **2017**, *29* (46), 1703852. https://doi.org/10.1002/adma.201703852.

(13) Odysseas Kosmatos, K.; Theofylaktos, L.; Giannakaki, E.; Deligiannis, D.; Konstantakou, M.; Stergiopoulos, T. Methylammonium Chloride: A Key Additive for Highly Efficient,

Stable, and Up-Scalable Perovskite Solar Cells. *ENERGY Environ. Mater.* **2019**, *2* (2), 79–92. https://doi.org/10.1002/eem2.12040.

(14) Guaita, M. G. D.; Szostak, R.; da Silva, F. M. C.; de Morais, A.; Moral, R. F.; Kodalle, T.; Teixeira, V. C.; Sutter-Fella, C. M.; Tolentino, H. C. N.; Nogueira, A. F. Influence of Methylammonium Chloride on Wide-Bandgap Halide Perovskites Films for Solar Cells. *Adv. Funct. Mater. n/a* (n/a), 2307104. https://doi.org/10.1002/adfm.202307104.

(15) Bi, L.; Fu, Q.; Zeng, Z.; Wang, Y.; Lin, F. R.; Cheng, Y.; Yip, H.-L.; Tsang, S. W.; Jen, A. K.-Y. Deciphering the Roles of MA-Based Volatile Additives for α-FAPbI3 to Enable Efficient Inverted Perovskite Solar Cells. *J. Am. Chem. Soc.* **2023**, *145* (10), 5920–5929. https://doi.org/10.1021/jacs.2c13566.

(16) Kim, M.; Kim, G.-H.; Lee, T. K.; Choi, I. W.; Choi, H. W.; Jo, Y.; Yoon, Y. J.; Kim, J. W.; Lee, J.; Huh, D.; Lee, H.; Kwak, S. K.; Kim, J. Y.; Kim, D. S. Methylammonium Chloride Induces Intermediate Phase Stabilization for Efficient Perovskite Solar Cells. *Joule* **2019**, *3* (9), 2179–2192. https://doi.org/10.1016/j.joule.2019.06.014.

(17) Valenzano, V.; Cesari, A.; Balzano, F.; Milella, A.; Fracassi, F.; Listorti, A.; Gigli, G.; Rizzo, A.; Uccello-Barretta, G.; Colella, S. Methylammonium-Formamidinium Reactivity in Aged Organometal Halide Perovskite Inks. *Cell Rep. Phys. Sci.* **2021**, *2* (5), 100432. https://doi.org/10.1016/j.xcrp.2021.100432.

(18) Wang, X.; Fan, Y.; Wang, L.; Chen, C.; Li, Z.; Liu, R.; Meng, H.; Shao, Z.; Du, X.; Zhang, H.; Cui, G.; Pang, S. Perovskite Solution Aging: What Happened and How to Inhibit? *Chem* **2020**, *6* (6), 1369–1378. https://doi.org/10.1016/j.chempr.2020.02.016.

(19) Palmer, J. R.; Iwamoto, S.; Han, C.; Dolan, C. J.; Vossler, H. M.; Dunfield, S. P.; Fenning, D. P. Problems with Solutions: Manipulating Alkylammonium Additive Reactivity for Durable High-Quality Perovskite Films. *New J. Chem.* **2024**. https://doi.org/10.1039/D4NJ03915G.

(20) Lin, H.; Zhou, C.; Tian, Y.; Siegrist, T.; Ma, B. Low-Dimensional Organometal Halide Perovskites. *ACS Energy Lett.* **2018**, *3* (1), 54–62. https://doi.org/10.1021/acsenergylett.7b00926.

(21) Lee, S. H.; Hong, S.; Kim, H. J. Selection of a Suitable Solvent Additive for 2-Methoxyethanol-Based Antisolvent-Free Perovskite Film Fabrication. *ACS Appl. Mater. Interfaces* **2022**, *14* (34), 39132–39140. https://doi.org/10.1021/acsami.2c10171.

(22) Lee, S. H.; Hong, S.; Yoon, G.; Kim, J. woo; Lee, H. H.; Kim, H. J. Crystallization Dynamics Control in Perovskite Films Using Alkylamines as Additives in a 2-Methoxyethanol-Based Antisolvent Free Process. *Mater. Today Energy* **2024**, *41*, 101516. https://doi.org/10.1016/j.mtener.2024.101516.

(23) Wu, X.; Zheng, Y.; Liang, J.; Tian, C.; Sun, A.; Tang, C.; Liu, Y.; Zhang, S.; Wang, C.; Song, S.; Chen, C.-C.; Reddy, K. M. Synergistic Effect of Alkylammonium Chlorides to Trigger an Ultrafast Nucleation for Antisolvent-Free Perovskite Solar Cells Processed from 2-Methoxyethanol. *Adv. Energy Mater.* **2024**, *14* (18), 2304302. https://doi.org/10.1002/aenm.202304302.

(24) Szostak, R.; de Souza Gonçalves, A.; de Freitas, J. N.; Marchezi, P. E.; de Araújo, F. L.; Tolentino, H. C. N.; Toney, M. F.; das Chagas Marques, F.; Nogueira, A. F. In Situ and Operando Characterizations of Metal Halide Perovskite and Solar Cells: Insights from Lab-Sized Devices to Upscaling Processes. *Chem. Rev.* **2023**, *123* (6), 3160–3236. https://doi.org/10.1021/acs.chemrev.2c00382.

(25) Kodalle, T.; Byranvand, M. M.; Goudreau, M.; Das, C.; Roy, R.; Kot, M.; Briesenick, S.; Zohdi, M.; Rai, M.; Tamura, N.; Flege, J. I.; Hempel, W.; Sutter-Fella, C. M.; Saliba, M. An Integrated Deposition and Passivation Strategy for Controlled Crystallization of 2D/3D Halide Perovskite Films. *Adv. Mater.* **2024**, *36* (24), 2309154. https://doi.org/10.1002/adma.202309154.

(26) Hoffman, J. M.; Strzalka, J.; Flanders, N. C.; Hadar, I.; Cuthriell, S. A.; Zhang, Q.; Schaller, R. D.; Dichtel, W. R.; Chen, L. X.; Kanatzidis, M. G. In Situ Grazing-Incidence Wide-Angle Scattering Reveals Mechanisms for Phase Distribution and Disorientation in 2D Halide Perovskite Films. *Adv. Mater.* **2020**, *32* (33), 2002812. https://doi.org/10.1002/adma.202002812.

(27) Sun, K.; Guo, R.; Liu, S.; Guo, D.; Jiang, X.; Huber, L. F.; Liang, Y.; Reus, M. A.; Li, Z.; Guan, T.; Zhou, J.; Schwartzkopf, M.; Stranks, S. D.; Deschler, F.; Müller-Buschbaum, P. Deciphering Structure and Charge Carrier Behavior in Reduced-Dimensional Perovskites. *Adv. Funct. Mater.* **2024**, *34* (52), 2411153. https://doi.org/10.1002/adfm.202411153.

(28) Ashiotis, G.; Deschildre, A.; Nawaz, Z.; Wright, J. P.; Karkoulis, D.; Picca, F. E.; Kieffer, J. The Fast Azimuthal Integration Python Library: pyFAI. *J. Appl. Crystallogr.* **2015**, *48* (2), 510–519. https://doi.org/10.1107/S1600576715004306.

(29) Kour, R.; Arya, S.; Verma, S.; Gupta, J.; Bandhoria, P.; Bharti, V.; Datt, R.; Gupta, V. Potential Substitutes for Replacement of Lead in Perovskite Solar Cells: A Review. *Glob. Chall.* **2019**, *3* (11), 1900050. https://doi.org/10.1002/gch2.201900050.

(30) Handayani, Y. S.; Indari, E. D.; Hidayat, R.; Othsubo, Y.; Kimura, S. Understanding the Role of Organic Cations on the Electronic Structure of Lead Iodide Perovskite from Their UV Photoemission Spectra and Their Electronic Structures Calculated by DFT Method. *Mater. Res. Express* **2019**, *6* (8), 084009. https://doi.org/10.1088/2053-1591/ab1d3f.

(31) Ramos-Terrón, S.; Verdugo-Escamilla, C.; Camacho, L.; de Miguel, G. A-Site Cation Engineering in 2D Ruddlesden–Popper (BA)2(MA1-A)2Pb3I10 Perovskite Films. *Adv. Opt. Mater.* **2021**, *9* (18), 2100114. https://doi.org/10.1002/adom.202100114.

(32) Szostak, R.; Marchezi, P. E.; Marques, A. dos S.; da Silva, J. C.; de Holanda, M. S.; Soares, M. M.; Tolentino, H. C. N.; Nogueira, A. F. Exploring the Formation of Formamidinium-Based Hybrid Perovskites by Antisolvent Methods: *In Situ* GIWAXS Measurements during Spin Coating. *Sustain. Energy Fuels* **2019**, *3* (9), 2287–2297. https://doi.org/10.1039/C9SE00306A.

(33) Munir, R.; Sheikh, A. D.; Abdelsamie, M.; Hu, H.; Yu, L.; Zhao, K.; Kim, T.; Tall, O. E.; Li, R.; Smilgies, D.-M.; Amassian, A. Hybrid Perovskite Thin-Film Photovoltaics: In Situ Diagnostics and Importance of the Precursor Solvate Phases. *Adv. Mater.* **2017**, *29* (2), 1604113. https://doi.org/10.1002/adma.201604113.

(34) Szostak, R.; Sanchez, S.; Marchezi, P. E.; Marques, A. S.; Silva, J. C.; Holanda, M. S.; Hagfeldt, A.; Tolentino, H. C. N.; Nogueira, A. F. Revealing the Perovskite Film Formation Using the Gas Quenching Method by In Situ GIWAXS: Morphology, Properties, and Device Performance. *Adv. Funct. Mater.* **2021**, *31* (4), 2007473. https://doi.org/10.1002/adfm.202007473.

(35) Cao, J.; Jing, X.; Yan, J.; Hu, C.; Chen, R.; Yin, J.; Li, J.; Zheng, N. Identifying the Molecular Structures of Intermediates for Optimizing the Fabrication of High-Quality Perovskite Films. *J. Am. Chem. Soc.* **2016**, *138* (31), 9919–9926. https://doi.org/10.1021/jacs.6b04924.

(36) Cheng, F.; Jing, X.; Chen, R.; Cao, J.; Yan, J.; Wu, Y.; Huang, X.; Wu, B.; Zheng, N. N-Methyl-2-Pyrrolidone as an Excellent Coordinative Additive with a Wide Operating Range for Fabricating High-Quality Perovskite Films. *Inorg. Chem. Front.* **2019**, *6* (9), 2458–2463. https://doi.org/10.1039/C9QI00547A.

(37) Park, B.; Kwon, H. W.; Lee, Y.; Lee, D. Y.; Kim, M. G.; Kim, G.; Kim, K.; Kim, Y. K.; Im, J.; Shin, T. J.; Seok, S. I. Stabilization of Formamidinium Lead Triiodide α-Phase with Isopropylammonium Chloride for Perovskite Solar Cells. *Nat. Energy* **2021**, *6* (4), 419–428. https://doi.org/10.1038/s41560-021-00802-z.

(38) Petrov, A. A.; Sokolova, I. P.; Belich, N. A.; Peters, G. S.; Dorovatovskii, P. V.; Zubavichus, Y. V.; Khrustalev, V. N.; Petrov, A. V.; Grätzel, M.; Goodilin, E. A.; Tarasov, A. B. Crystal Structure of DMF-Intermediate Phases Uncovers the Link Between CH3NH3PbI3 Morphology and Precursor Stoichiometry. *J. Phys. Chem. C* **2017**, *121* (38), 20739–20743. https://doi.org/10.1021/acs.jpcc.7b08468.

(39) Wu, C.; Wang, D.; Zhang, Y.; Gu, F.; Liu, G.; Zhu, N.; Luo, W.; Han, D.; Guo, X.; Qu, B.; Wang, S.; Bian, Z.; Chen, Z.; Xiao, L. FAPbI3 Flexible Solar Cells with a Record Efficiency of 19.38% Fabricated in Air via Ligand and Additive Synergetic Process. *Adv. Funct. Mater.* **2019**, *29* (34), 1902974. https://doi.org/10.1002/adfm.201902974.

(40) Nan, Z.-A.; Chen, L.; Liu, Q.; Wang, S.-H.; Chen, Z.-X.; Kang, S.-Y.; Ji, J.-B.; Tan, Y.-Y.; Hui, Y.; Yan, J.-W.; Xie, Z.-X.; Liang, W.-Z.; Mao, B.-W.; Tian, Z.-Q. Revealing Phase Evolution Mechanism for Stabilizing Formamidinium-Based Lead Halide Perovskites by a Key Intermediate Phase. *Chem* **2021**, *7* (9), 2513–2526. https://doi.org/10.1016/j.chempr.2021.07.011.

(41) Chen, L.; Hu, M.; Risqi, A. M.; Noh, E.; Lee, Y.; Seok, S. I. Unraveling the Influence of Solvent on Side Reactions between Formamidinium Lead Triiodide and Methylammonium Cations. *J. Am. Chem. Soc.* **2024**, *146* (14), 10159–10166. https://doi.org/10.1021/jacs.4c01779.

(42) Vasileiadou, E. S.; Wang, B.; Spanopoulos, I.; Hadar, I.; Navrotsky, A.; Kanatzidis, M. G. Insight on the Stability of Thick Layers in 2D Ruddlesden–Popper and Dion–Jacobson Lead Iodide Perovskites. *J. Am. Chem. Soc.* **2021**, *143* (6), 2523–2536. https://doi.org/10.1021/jacs.0c11328.

(43) Kim, H.; Yoo, S.-M.; Ding, B.; Kanda, H.; Shibayama, N.; Syzgantseva, M. A.; Tirani, F. F.; Schouwink, P.; Yun, H. J.; Son, B.; Ding, Y.; Kim, B.-S.; Kim, Y. Y.; Park, J.; Syzgantseva,

O. A.; Jeon, N. J.; Dyson, P. J.; Nazeeruddin, M. K. Shallow-Level Defect Passivation by 6H Perovskite Polytype for Highly Efficient and Stable Perovskite Solar Cells. *Nat. Commun.* **2024**, *15* (1), 5632. https://doi.org/10.1038/s41467-024-50016-6.

The data supporting this article have been included as part of the Supplementary Information.